Cluster radioactivity of _{118}^{294}Og_{176}

Zachary Matheson, Samuel A. Giuliani, Witold Nazarewicz, Jhilam Sadhukhan, and Nicolas Schunck

Phys. Rev. C **99**, 041304 — Published 29 April 2019

DOI: 10.1103/PhysRevC.99.041304

Cluster radioactivity of $^{294}_{118}Og_{176}$

Zachary Matheson,[1] Samuel Giuliani,[1] Witold Nazarewicz,[1] Jhilam Sadhukhan,[2,3] and Nicolas Schunck[4]

[1]*Department of Physics and Astronomy and FRIB Laboratory, Michigan State University, East Lansing, Michigan 48824, USA*
[2]*Variable Energy Cyclotron Centre, Kolkata 700064*
[3]*Homi Bhabha National Institute, Mumbai 400094, India*
[4]*Nuclear and Chemical Science Division, Lawrence Livermore National Laboratory, Livermore, California 94551, USA*

(Dated: March 14, 2019)

According to theory, cluster radioactivity becomes an important decay mode in superheavy nuclei. In this work, we predict that the strongly-asymmetric fission, or cluster emission, is in fact the dominant fission channel for $^{294}_{118}Og_{176}$, which is currently the heaviest synthetic isotope known. Our theoretical approach incorporates important features of fission dynamics, including quantum tunneling and stochastic dynamics up to scission. We show that, despite appreciable differences in static fission properties such as fission barriers and spontaneous fission lifetimes, the prediction of cluster radioactivity in $^{294}_{118}Og_{176}$ is robust with respect to the details of calculations, including the choice of energy density functional, collective inertia, and the strength of the dissipation term.

Introduction – The region of superheavy nuclei ($Z \geq 104$) is one of the frontiers of modern nuclear physics. The heavy-ion fusion experiments have been able to push the boundaries of the nuclear chart all the way to $^{294}_{118}Og_{176}$ [1–3], and new efforts are underway to increase production rates of superheavy systems [4–7]. Due to the large number of nucleons, these nuclei push the limits of nuclear structure models and are expected to answer key questions pertaining to nuclear and atomic physics, astrophysics, and chemistry [8–11]. For instance, since the liquid drop model predicts vanishing fission barriers for superheavy elements due to the strong Coulomb repulsion, shell effects become absolutely essential and spontaneous fission ends up governing the lifetimes of many of these new systems [12, 13]. The fission of superheavy elements may also play an important role in the astrophysical r process, by placing an endpoint on neutron capture and through the fission cycling [14].

In the superheavy research enterprise, theory plays a critical role by guiding experiments, interpreting their results, and making predictions in the regions that cannot be reached experimentally [10, 11] because of huge proton and neutron numbers involved. In these extreme regions, it is important to use models of spontaneous (or low-energy) fission rooted firmly in many-body quantum mechanics. To this end, microscopic models based on density functional theory (DFT) where collective dynamics is decoupled from underlying intrinsic excitations offer a path which is computationally tractable, while still maintaining a direct link to the underlying quantum many-body problem [15]. These models can be used to predict observables such as half-lives [15–21] and primary fragment yields [22–25] within the same theoretical framework.

In this work, we discuss an exotic form of cold highly-asymmetric fission, known in the literature as cluster radioactivity or cluster emission [26–28], which we predict is the dominant form of fission in the superheavy isotope $^{294}_{118}Og_{176}$. Cluster emission, an intermediate process between α decay and conventional fission with fragments of more comparable masses, occurs when a parent nucleus decays into a large fragment near doubly-magic $^{208}_{82}Pb_{126}$ and a lighter cluster. It has been observed experimentally in actinides, starting with the $^{223}_{88}Ra \rightarrow ^{209}_{82}Pb + ^{14}_{6}C$ decay [29]. It is always a rare event with a small branching ratio [30]. From the theoretical point of view, half-life calculations based on semiempirical models predict cluster radioactivity to be the dominant decay channel of several superheavy nuclei [31–37]. Similar predictions have been obtained by more microscopic calculations using nuclear DFT framework [23, 38]. However, so far no determination of fission yields has been made that explicitly demonstrates the emergence of cluster radioactivity in superheavy elements, either theoretically or experimentally. In this paper, which extends the discussion of recent Ref. [23] to fission yields, we calculate spontaneous fission yields of $^{294}_{118}Og_{176}$ and explicitly predict for the first time that cluster emission is dramatically enhanced to the point that it becomes the primary spontaneous fission channel.

Our paper is organized as follows. First, we briefly sketch the microscopic DFT+Langevin framework used to calculate fission fragment distributions. We then compute the spontaneous fission characteristics of $^{294}_{118}Og_{176}$. Finally, we study the robustness of our fission yield predictions with respect to different energy density functionals (EDFs), collective spaces, collective inertias, and dissipation.

Model – We calculate fission fragment distributions following the approach described in Ref.[22], which may be divided into two stages. In the first stage, we use the semiclassical WKB approximation to model spontaneous fission as quantum tunneling through a multidimensional potential energy surface (PES) characterized by N collective coordinates $\mathbf{q} \equiv (q_1, \ldots, q_N)$. In our implementation of the WKB approximation, the most-probable tunneling

path $L(s)|_{s_{\rm in}}^{s_{\rm out}}$ in the collective space is found via minimization of the collective action

$$S(L) = \frac{1}{\hbar}\int_{s_{\rm in}}^{s_{\rm out}} \sqrt{2\mathcal{M}(s)\,(V(s)-E_0)}ds, \qquad (1)$$

where s is the curvilinear coordinate along the path L, $\mathcal{M}(s)$ is the collective inertia [39] and $V(s)$ is the potential energy along $L(s)$. E_0 stands for the collective ground-state energy. The dynamic programming method [40] is employed to determine the path $L(s)$. The calculation is repeated for different outer turning points, and each of these points is then assigned an exit probability $P(s_{\rm out}) = [1+\exp(2S)]^{-1}$ [41].

In the second stage, fission trajectories begin from the outer turning line and then evolve along the PES according to the Langevin equations:

$$\begin{aligned}\frac{dp_i}{dt} =& -\frac{p_j p_k}{2}\frac{\partial}{\partial q_i}\left(\mathcal{M}^{-1}\right)_{jk} - \frac{\partial V}{\partial q_i}\\ &- \eta_{ij}\left(\mathcal{M}^{-1}\right)_{jk} p_k + g_{ij}\Gamma_j(t)\,, \qquad (2)\\ \frac{dq_i}{dt} =& \left(\mathcal{M}^{-1}\right)_{ij} p_j\,,\end{aligned}$$

where p_i is the collective momentum conjugate to q_i. The dissipation tensor η_{ij} is related to the random force strength g_{ij} via the fluctuation-dissipation theorem, and $\Gamma_j(t)$ is a Gaussian-distributed, time-dependent stochastic variable. All trajectories ending at a particular scission configuration are weighted with the appropriate $P(s_{\rm out})$. These scission configurations were defined based on the expectation value of the neck operator $Q_N = e^{-(z-z_n)^2/a_n^2}$, setting $a_n = 1$ fm and with z_n, taken to be the point in the nucleus with the lowest density, describing the position of the neck. We defined our scission line differently for each functional that was used, with the value $Q_N = 7$ for UNEDF1$_{\rm HFB}$ and SkM* and $Q_N = 9$ for D1S. Particle number fluctuations in the neck at or near the scission line were accounted for by convoluting our Langevin yields with a Gaussian function of width $\sigma_A = 6$ for A and $\sigma_Z = 4$ for Z.

The key ingredients in these calculations, V and $\mathcal{M}$, are calculated self-consistently by solving the Hartree-Fock-Bogoliubov equations employing Skyrme and Gogny EDFs. To evaluate the robustness of our results with respect to different inputs, we perform calculations using three distinct EDFs: UNEDF1$_{\rm HFB}$[42], a Skyrme functional which was optimized to data for spherical and deformed nuclei, including fission isomers; SkM* [43], another Skyrme functional designed for fission barriers and surface energy; and D1S [44], a parametrization of the finite-range Gogny interaction fitted on fission barriers of actinides.

In self-consistent fission models, the lowest multipole moments characterizing nuclear shape deformations are usually selected as collective coordinates. The remaining shape degrees of freedom are, in principle, decided through the energy minimization. In the present work, axial quadrupole moment Q_{20}, triaxial quadrupole moment Q_{22}, and axial octupole moment Q_{30} are considered as collective coordinates since the fission dynamics associated with fragment-yield distributions is mostly confined within this deformation space. Additionally, pairing correlations have a strong impact on the spontaneous fission half-lives calculated via action minimization [19, 45, 46]. It is taken into account through the coordinate λ_2 representing dynamic pairing fluctuations [45]. To obtain $S(L)$, a dimensionless collective space is introduced as in Ref. [45].

To balance computational speed with complexity, we used a different collective space for each functional. The most detailed calculation was carried out using UNEDF1$_{\rm HFB}$ in a four dimensional space $(Q_{20}, Q_{22}, Q_{30}, \lambda_2)$. Calculations were performed using the symmetry-unrestricted DFT solver HFODD [47]. To assure good convergence, we used the 1500 lowest single particle levels corresponding to 30 stretched harmonic oscillator shells.

The analysis of the four-dimensional (4D) PES showed that Q_{30} remains negligible through the first saddle point (up to at least $Q_{20} = 100$ b), and that Q_{22} and λ_2 are unimportant beyond the outer turning-point hypersurface. This allowed us to simplify calculations with other functionals. The SkM* calculations were performed in a piecewise space ($(Q_{20}, Q_{22}, \lambda_2)$ up to the fission isomer, $(Q_{20}, Q_{30}, \lambda_2)$ from fission isomer to outer turning points, and (Q_{20}, Q_{30}) beyond the outer turning-point line) with the same pairing properties as given in [39, 45, 48], and the same HFODD basis as in UNEDF1$_{\rm HFB}$ calculations. The PES connection at the fission isomer assumed $Q_{22} = Q_{30} = 0$, with Q_{20} and λ_2 continued smoothly, as in [22]. In the case of Gogny D1S calculations, a two-dimensional collective space described by coordinates (Q_{20}, Q_{30}) was used within the DFT solver HFBaxial [49], where the stretched harmonic oscillator basis corresponding to 17 harmonic oscillator shells was optimized for each (Q_{20}, Q_{30}) value. Each PES was interpolated from a discrete, uniform grid, the spacing of which is shown in the upper half of Table I.

Several approximations are commonly used to compute the collective inertia, which describes the tendency of the nucleus to resist configuration changes. The most accurate prescription available to date is obtained from non-perturbative cranking approximation to the adiabatic time-dependent Hartree-Fock-Bogoliubov (ATDHFB) inertia ($\mathcal{M}^{\rm A}$) [50]. On the other hand, perturbative expressions prioritize computational simplicity by sacrificing details of the level crossing dynamics, which results in a smoothed-out collective inertia. We also performed calculations using both the perturbative cranking ATDHFB inertia ($\mathcal{M}^{\rm AP}$) [50] and the perturbative GCM inertia ($\mathcal{M}^{\rm GCM}$) [15], which has the same structure as $\mathcal{M}^{\rm AP}$ but with an absolute magnitude quenched by a factor

TABLE I. Top: Mesh sizes used for the discretization of the potential energy surface. Bottom: Step sizes used in the calculation of the non-perturbative inertia $\mathcal{M}^{\rm A}$.

	WKB region				Langevin region	
	ΔQ_{20} (b)	ΔQ_{22} (b)	ΔQ_{30} ($b^{3/2}$)	$\Delta\lambda_2$ (MeV)	ΔQ_{20} (b)	ΔQ_{30} ($b^{3/2}$)
UNEDF1$_{\rm HFB}$	6	3	3	0.05	4	2
SkM*	4	-	2	0.05	4	2
D1S	4	-	2.5	-	4	2.5
UNEDF1$_{\rm HFB}$	6	3	3	0.05	0.001	0.001
SkM*	4	-	2	0.05	0.001	0.001
D1S	0.1	-	0.1	-	0.1	0.1

1.5 [51]. In UNEDF1$_{\rm HFB}$ and SkM* the derivatives were computed by means of the Lagrange three-point formula for unequally spaced points (see Ref. [50]), while first order finite difference formulas were used for D1S (see Ref. [51]). A summary of the step sizes used in the calculation of $\mathcal{M}^{\rm A}$ for each collective variable and region of the PES is given in the lower half of Table I.

In this work, we set the dissipation strength η_{ij} as an adjustable parameter rather than using some of the common prescriptions [52, 53], which have not yet been adapted to DFT inputs. We examined the sensitivity of our calculations to η_{ij} by varying it around the baseline value used in [22]: $\boldsymbol{\eta}_0 \equiv (\eta_{22}, \eta_{23}, \eta_{33}) \equiv (50\hbar, 5\hbar, 40\hbar)$.

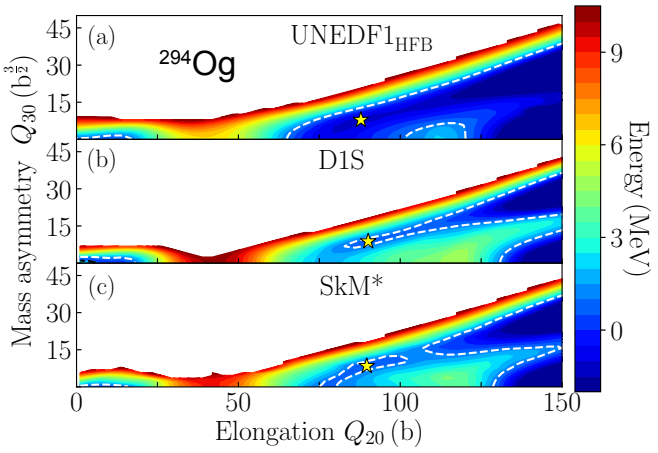

FIG. 1. Comparison of the PESs for $^{294}_{118}$Og$_{176}$ in the (Q_{20}, Q_{30}) collective plane obtained in UNEDF1$_{\rm HFB}$ (a), D1S (b), and SkM* (c) EDFs. The ground-state energy E_{gs} is normalized to zero. The dotted line in each figure corresponds to $E_0 - E_{gs} = 1$ MeV, which was used to determine the inner and outer turning points. The local energy minima at large deformations are marked by stars.

Results – We first compare in Fig. 1 the two-dimensional PESs in the (Q_{20}, Q_{30}) plane for the functionals UNEDF1$_{\rm HFB}$, D1S, and SkM*. There we notice that the overall topology of the PES is roughly similar in all models, with a symmetric saddle point occurring around $Q_{20} \approx 40$ b, a second barrier beginning around $Q_{20} \approx 100 - 120$ b along the symmetric fission path, the presence of local minima at large deformations, a deep valley that leads to an highly-asymmetric split, and the secondary less-asymmetric fission valley that emerges at large elongations.

But there are differences as well, such as the height of the first saddle point, the depth of the highly-asymmetric fission valley, and the height of the ridge separating the two fission valleys. As a result, the outer turning points are pushed to larger elongations in D1S and SkM* as compared to UNEDF1$_{\rm HFB}$. These differences in the PES topology strongly affect the predicted spontaneous fission half-lives $\tau_{\rm SF}$, which in the case of UNEDF1$_{\rm HFB}$, SkM* and D1S are 9.1×10^{-9} s, 4.0×10^{-5} s and 3.2×10^{-2} s, respectively (see also [13, 17] for a detailed discussion of half-lives). These large variations of $\tau_{\rm SF}$ reflect the well-known exponential sensitivity of spontaneous fission half-lives to changes in the quantities entering the collective action (1). The $\tau_{\rm SF}$ predictions of UNEDF1$_{\rm HFB}$ and, to a lesser degree, SkM* are incompatible with experiment, as ^{294}Og is known to decay by α-decay with a half-life of 0.58 ms [3]. This observation could in fact also apply to the D1S results, since the D1S calculations were performed in a smaller collective space leading to overestimation of the half-lives [19, 45]. It is to be noted that while half-lives are very sensitive to details of the calculations, the models used in this study are very consistent with each other and with experiment when it comes to global observables, such as alpha-decay energies, deformations, and radii [11, 54]. As demonstrated below, spontaneous-fission mass and charge yields are also robustly predicted.

Despite the strong variations in the predicted $\tau_{\rm SF}$, we see in Fig. 2 that the predicted fission yields are in fact rather independent of the EDF choice. Namely, all three functionals predict a heavy fragment in the neighborhood of $^{208}_{82}$Pb$_{126}$ and a light fragment near $^{86}_{36}$Kr$_{50}$.

The sensitivity to the different inputs are shown in Fig. 3 through one-dimensional projections onto the fragment mass and charge. The top panels of Fig. 3 shows again that all three functionals predict highly-asymmetric fission with the heavy fragment centered at or around $^{208}_{82}$Pb$_{126}$. While the peaks corresponding to the D1S and SkM* functionals overlap quite well, the UNEDF1$_{\rm HFB}$ distributions (both in 2D and 4D space) are broader and shifted slightly towards more asymmetric splits. This may be related to the relative flatness of the UNEDF1$_{\rm HFB}$ PES compared to the others, which makes it more susceptible to large fluctuations. The secondary tiny peak around $^{126}_{54}$Xe$_{72}$ predicted by SkM*, associated with the more symmetric fission valley of Fig. 1(c) is clearly seen. For D1S and UNEDF1$_{\rm HFB}$, the yield distributions do not show a tail at lower masses/charges. As discussed below, this can be associated with both the

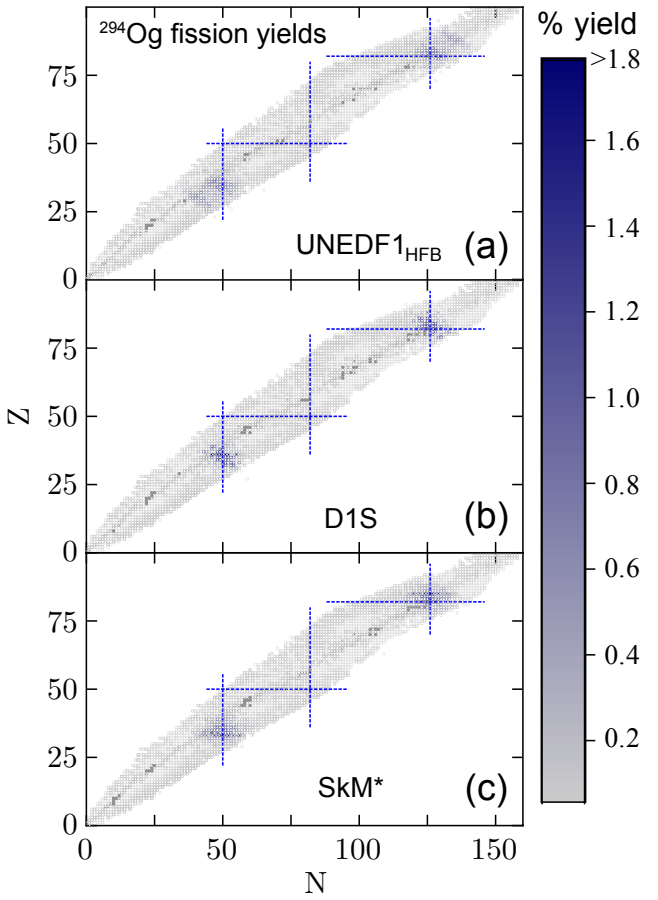

FIG. 2. Fission fragment distributions for $^{294}_{118}\mathrm{Og}_{176}$ obtained in UNEDF1$_{\mathrm{HFB}}$ (a), D1S (b), and SkM* (c) EDFs using the non-perturbative cranking ATDHFB inertia and the baseline dissipation tensor $\boldsymbol{\eta}_0$. Known isotopes are marked in grey [55]. Magic numbers 50, 82, and 126 are indicated by dotted lines.

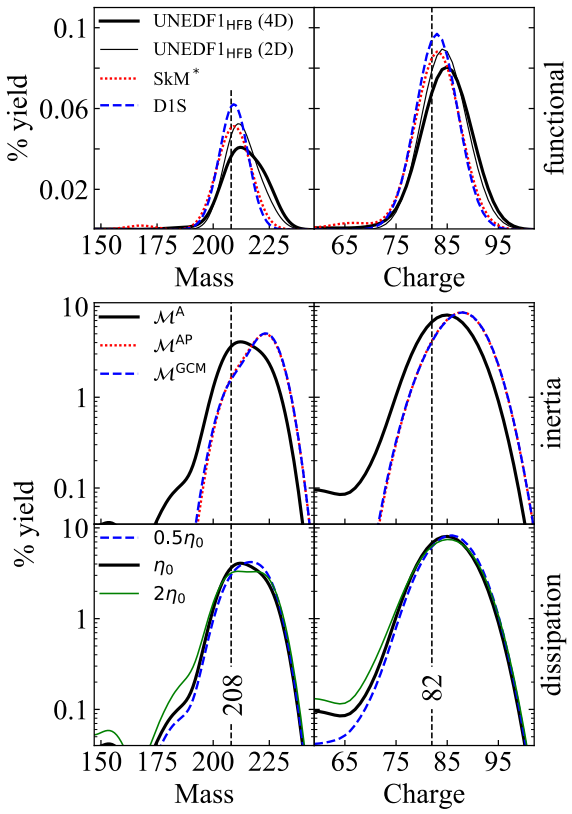

FIG. 3. Upper panel: Predicted heavy fragment mass (left) and charge (right) yields of $^{294}_{118}\mathrm{Og}_{176}$ using different functionals (top, linear scale). Bottom panels: collective inertias and dissipation tensor strengths (in logarithmic scale). The baseline calculation was performed using the UNEDF1$_{\mathrm{HFB}}$ functional in a 4D space with non-perturbative cranking ATDHFB inertia and dissipation tensor strength $\boldsymbol{\eta}_0$.

collective inertia and the energy ridge (particularly pronounced for D1S), both effectively separating the two fission valleys.

The impact of the choice of collective inertia on the fission yield distributions is illustrated in the middle panels of Fig. 3. While recent time-dependent DFT work on induced fission has played down the role of collective inertia [56] outside the barrier, it was emphasized in Ref. [22] that the tunneling phase of spontaneous fission was highly sensitive to it. This may explain the fine deviations observed in Fig. 3. The yields corresponding to $\mathcal{M}^{\mathrm{AP}}$ and $\mathcal{M}^{\mathrm{GCM}}$ overlap and both are shifted towards more asymmetric splits compared to $\mathcal{M}^{\mathrm{A}}$. This suggests that it is the topology of the collective inertia, rather than its absolute magnitude, which affects the shape of the fission yields. In particular, we find that the smoothness of the perturbative inertia allows fluctuations to diffuse the yield to more extreme fragment configurations.

The bottom panels of Fig. 3 show the effect of varying the strength of the dissipation tensor. This parameter has a noticeable impact on the yields, particularly on the tails and the yields associated with the more-symmetric channel. The results corresponding to $\boldsymbol{\eta} = \boldsymbol{\eta}_0, 0.5\boldsymbol{\eta}_0$, and $2\boldsymbol{\eta}_0$ are very close. This is consistent with findings of Refs. [57–59], which found that the yield distributions are not very sensitive to the precise value of the dissipation tensor. In general, irrespective of the choice of energy density functional, we found a rather similar pattern of yield distributions with respect to the inertia tensor and the dissipation strength. Only at the extreme limits of constant inertia and no dissipation do we see an increase of the symmetric peak in the predicted yields. However, as discussed in [39, 45, 58–60], such choices are not realistic. For this reason, we have not included them in the figure and mention them only for the sake of completeness.

Finally, to better understand the formation of the most-probable fission fragments, we studied the nucleon localization functions [59, 61] along the cluster-decay path. As shown in Fig. 4, by comparing the $^{294}_{118}\mathrm{Og}_{176}$

localizations with those calculated for spherical $^{208}_{82}Pb_{126}$ and $^{86}_{36}Kr_{50}$, we found that both the lead prefragment and the $N \approx 50$ neutrons belonging to krypton are well-localized. This result highlights the importance of shell structure along the fission path in determining the most probable fragment configuration in fissioning nuclei. It is interesting to note that the neutron localizations in the highly elongated configurations of $^{294}_{118}Og_{176}$ shown in the left panels of Fig. 4 have much more structure than the ground-state localizations, which are close to the Fermi-gas limit [9]. Indeed, the single-particle level density is very high in $^{294}_{118}Og_{176}$, which is not the case for the prefragments.

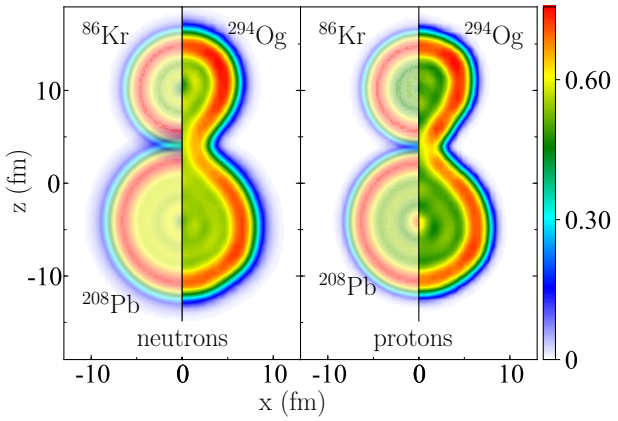

FIG. 4. Nucleon localization function for a highly-deformed configuration of $^{294}_{118}Og_{176}$, $(Q_{20}, Q_{30}) = (264\,\mathrm{b}, 60\,\mathrm{b}^{3/2})$ for neutrons (left panels) and protons (right panels). For comparison, localizations are shown for the prefragments $^{208}_{82}Pb_{126}$ and $^{86}_{36}Kr_{50}$ on the left side of each subplot.

Conclusions – In this paper, which reinforces the results of Ref. [23], we predict that the dominant spontaneous fission mode of $^{294}_{118}Og_{176}$ will be a highly-asymmetric cluster emission sharply centered around doubly-magic $^{208}_{82}Pb_{126}$ and magic $^{86}_{36}Kr_{50}$. We have shown that this prediction is fairly robust with respect to the choice of input parameters, such as energy density functional, collective inertia, and dissipation tensor. In particular, we emphasize that differences in barrier heights predicted by different EDFs do not affect the calculated fission yields. We confirmed the implicit assumption of [22], that 4D calculations do not necessarily offer an improved description of the tunneling compared to a well-chosen 3D description, and we argue for a hierarchy of ingredients necessary for a Langevin description of low-energy fission.

The search for cluster emission has already begun [3]. Since, as demonstrated in this work, an asymmetric fission of $^{294}_{118}Og_{176}$ is expected to be strongly enhanced thus providing a strong experimental trigger, we are optimistic that the next generation of experiments, perhaps involving an ionization chamber [3], will find experimental evidence of cluster radioactivity of $^{294}_{118}Og_{176}$.

ACKNOWLEDGEMENTS

This work was supported by the U.S. Department of Energy under Award Numbers DOE-DE-NA0002847 (NNSA, the Stewardship Science Academic Alliances program), DE-SC0013365 (Office of Science), and DE-SC0018083 (Office of Science, NUCLEI SciDAC-4 collaboration). as well as by the Office of Science, Office of Workforce Development for Teachers and Scientists, Office of Science Graduate Student Research (SCGSR) program. The SCGSR program is administered by the Oak Ridge Institute for Science and Education (ORISE) for the DOE. ORISE is managed by ORAU under contract number DE-SC0014664. This work was also partly performed under the auspices of the US Department of Energy by the Lawrence Livermore National Laboratory under Contract DE-AC52-07NA27344. Computing support came from the Lawrence Livermore National Laboratory (LLNL) Institutional Computing Grand Challenge program.

[1] Y. T. Oganessian *et al.*, Phys. Rev. C **74**, 044602 (2006).
[2] Y. T. Oganessian *et al.*, Phys. Rev. Lett. **109**, 162501 (2012).
[3] N. Brewer *et al.*, Phys. Rev. C **98**, 024317 (2018).
[4] S. Dmitriev, M. Itkis, and Y. Oganessian, Eur. Phys. J. WOC **131**, 08001 (2016).
[5] Y. T. Oganessian and S. N. Dmitriev, Russ. Chem. Rev. **85**, 901 (2016).
[6] S. Hofmann *et al.*, Eur. Phys. J. A **52**, 180 (2016).
[7] J. B. Roberto and K. P. Rykaczewski, Sep. Sci. Technol. **53**, 1813 (2018).
[8] C. E. Düllmann and M. Block, Sci. Am. **318**, 48 (2018).
[9] P. Jerabek, B. Schuetrumpf, P. Schwerdtfeger, and W. Nazarewicz, Phys. Rev. Lett. **120**, 5 (2018).
[10] W. Nazarewicz, Nature Phys. **14**, 537 (2018).
[11] S. A. Giuliani, Z. Matheson, W. Nazarewicz, E. Olsen, P.-G. Reinhard, J. Sadhukhan, B. Schuetrumpf, N. Schunck, and P. Schwerdtfeger, Rev. Mod. Phys., in press (2019).
[12] F. P. Heßberger, Euro. Phys. J. A **53**, 75 (2017).
[13] A. Baran, M. Kowal, P. G. Reinhard, L. M. Robledo, A. Staszczak, and M. Warda, Nucl. Phys. A **944**, 442 (2015).
[14] S. A. Giuliani, G. Martínez-Pinedo, and L. M. Robledo, Phys. Rev. C **97**, 034323 (2018).
[15] N. Schunck and L. M. Robledo, Rep. Prog. Phys. **79**, 116301 (2016).
[16] J. Erler, K. Langanke, H. P. Loens, G. Martínez-Pinedo, and P.-G. Reinhard, Phys. Rev. C **85**, 025802 (2012).
[17] A. Staszczak, A. Baran, and W. Nazarewicz, Phys. Rev. C **87**, 024320 (2013).
[18] S. A. Giuliani and L. M. Robledo, Phys. Rev. C **88**, 054325 (2013).

[19] S. A. Giuliani, L. M. Robledo, and R. Rodríguez-Guzmán, Phys. Rev. C **90**, 054311 (2014).
[20] J.-F. Lemaître, S. Goriely, S. Hilaire, and N. Dubray, Phys. Rev. C **98**, 024623 (2018).
[21] R. Rodríguez-Guzmán and L. M. Robledo, Phys. Rev. C **98**, 034308 (2018).
[22] J. Sadhukhan, W. Nazarewicz, and N. Schunck, Phys. Rev. C **93**, 011304 (2016).
[23] M. Warda, A. Zdeb, and L. M. Robledo, Phys. Rev. C **98**, 041602 (2018).
[24] D. Regnier, N. Dubray, N. Schunck, and M. Verrière, Phys. Rev. C **93**, 054611 (2016).
[25] D. Regnier, N. Dubray, and N. Schunck, Phys. Rev. C **99**, 024611 (2019).
[26] A. Sandulescu, D. Poenaru, and W. Greiner, Sov. J. Part. Nuclei **11**, 528 (1980).
[27] D. Poenaru, W. Greiner, K. Depta, M. Ivascu, D. Mazilu, and A. Sandulescu, At. Data Nucl. Data Tables **34**, 423 (1986).
[28] G. Royer, R. K. Gupta, and V. Denisov, Nucl. Phys. A **632**, 275 (1998).
[29] H. J. Rose and G. A. Jones, Nature **307**, 245247 (1983).
[30] D. N. Poenaru and W. Greiner, in *Clusters in Nuclei: Volume 1*, edited by C. Beck (Springer Berlin Heidelberg, Berlin, Heidelberg, 2010) p. 1.
[31] D. N. Poenaru, R. A. Gherghescu, and W. Greiner, Phys. Rev. Lett. **107**, 062503 (2011).
[32] D. N. Poenaru, R. A. Gherghescu, and W. Greiner, Phys. Rev. C **85**, 034615 (2012).
[33] D. N. Poenaru, R. A. Gherghescu, and W. Greiner, J. Phys. Conf. Ser. **436**, 012056 (2013).
[34] D. N. Poenaru, R. A. Gherghescu, W. Greiner, and N. S. Shakib, in *Nuclear Physics: Present and Future* (Springer International Publishing, 2015) p. 131.
[35] D. N. Poenaru and R. A. Gherghescu, Phys. Rev. C **97**, 044621 (2018).
[36] K. P. Santhosh and C. Nithya, Phys. Rev. C **97**, 064616 (2018).
[37] Y. L. Zhang and Y. Z. Wang, Phys. Rev. C **97**, 014318 (2018).
[38] M. Warda and L. M. Robledo, Phys. Rev. C **84**, 044608 (2011).
[39] J. Sadhukhan, K. Mazurek, A. Baran, J. Dobaczewski, W. Nazarewicz, and J. A. Sheikh, Phys. Rev. C **88**, 064314 (2013).
[40] A. Baran, K. Pomorski, A. Łukasiak, and A. Sobiczewski, Nucl. Phys. A **361**, 83 (1981).
[41] A. Baran, Phys. Lett. B **76**, 8 (1978).
[42] N. Schunck, J. D. McDonnell, J. Sarich, S. M. Wild, and D. Higdon, J. Phys. G **42**, 34024 (2015).
[43] J. Bartel, P. Quentin, M. Brack, C. Guet, and H.-B. Håkansson, Nucl. Phys. A **386**, 79 (1982).
[44] J. Berger, M. Girod, and D. Gogny, Nucl. Phys. A **502**, 85 (1989).
[45] J. Sadhukhan, J. Dobaczewski, W. Nazarewicz, J. A. Sheikh, and A. Baran, Phys. Rev. C **90**, 061304 (2014).
[46] J. Zhao, B.-N. Lu, T. Nikšić, D. Vretenar, and S.-G. Zhou, Phys. Rev. C **93**, 044315 (2016).
[47] N. Schunck *et al.*, Comput. Phys. Commun. **216**, 145 (2017).
[48] J. D. Mcdonnell, W. Nazarewicz, J. A. Sheikh, A. Staszczak, and M. Warda, Phys. Rev. C **021302**, 18 (2014).
[49] Luis M. Robledo, code HFBaxial, 2002, `http://gamma.ft.uam.es/robledo/Downloads.html`.
[50] A. Baran, J. A. Sheikh, J. Dobaczewski, W. Nazarewicz, and A. Staszczak, Phys. Rev. C **84**, 054321 (2011).
[51] S. A. Giuliani and L. M. Robledo, Phys. Lett. B **787**, 134 (2018).
[52] M. D. Usang, F. A. Ivanyuk, C. Ishizuka, and S. Chiba, Phys. Rev. C **96**, 064617 (2017).
[53] C. Ishizuka, M. D. Usang, F. A. Ivanyuk, J. A. Maruhn, K. Nishio, and S. Chiba, Phys. Rev. C **96**, 064616 (2017).
[54] P.-H. Heenen, J. Skalski, A. Staszczak, and D. Vretenar, Nucl. Phys. A **944**, 415 (2015).
[55] Interactive Chart of Nuclides, NuDat 2.7 `https://www.nndc.bnl.gov/nudat2/`.
[56] A. Bulgac, S. Jin, K. Roche, N. Schunck, and I. Stetcu, ArXiv e-prints (2018), arXiv:1806.00694 [nucl-th].
[57] J. Randrup, P. Möller, and A. J. Sierk, Phys. Rev. C **84**, 034613 (2011).
[58] A. J. Sierk, Phys. Rev. C **96**, 034603 (2017).
[59] J. Sadhukhan, C. Zhang, W. Nazarewicz, and N. Schunck, Phys. Rev. C **061301**, 1 (2017).
[60] Y. Aritomo, S. Chiba, and F. Ivanyuk, Phys. Rev. C **90**, 054609 (2014).
[61] C. L. Zhang, B. Schuetrumpf, and W. Nazarewicz, Phys. Rev. C **94**, 1 (2016).